Journal of Materials Chemistry A

ROYAL SOCIETY OF CHEMISTRY

PAPER

View Article Online
View Journal | View Issue



Cite this: J. Mater. Chem. A, 2021, 9, 16878

# Rational surface engineering of MXene@N-doped hollow carbon dual-confined cobalt sulfides/selenides for advanced aluminum batteries†

Long Yao,‡ Shunlong Ju‡ and Xuebin Yu *

Rechargeable aluminum batteries (RABs) based on multivalent ion transfer have attracted great attention due to their large specific capacities, natural abundance, and high safety of metallic Al anodes. However, the poor cycling performance and sluggish diffusion kinetics severely restrict the development of RABs. In this paper, the mechanism of impacting the rechargeable ability of $Co_9S_8$ electrodes is demonstrated to be linked to the production of soluble active cobalt species upon both chemical dissolution and electrochemical conversion processes. To avoid the excessive loss of active species and structural pulverization, rational surface engineering of MXenes and N-doped hollow carbon dual-confined $Co_9S_8$ nanoparticle composites ($Co_9S_8$ NP@NPC@MXene) is designed to enhance the aluminum storage properties. The cell delivered a high reversible capacity (277 mA h $g^{-1}$ at 0.1 A $g^{-1}$ after 100 cycles), excellent rate-cycle capability up to 1 A $g^{-1}$, and low polarization. Furthermore, this strategy is also successfully demonstrated in a $CoSe_2$ electrode that presents a high discharge capacity of up to 288 mA h $g^{-1}$ at 1 A $g^{-1}$ as well as a desirable capacity retention of approximately 220 mA h $g^{-1}$ after 300 cycles, demonstrating its feasibility and versatility. This elaborate work would be of great significance for the further development of advanced chalcogenides for RAB cathodes.

Received 25th April 2021
Accepted 9th July 2021

DOI: 10.1039/d1ta03465k

rsc.li/materials-a



## Introduction

The extensive growth of electric vehicles and portable devices, as well as increasing concerns about safety, cost, and the natural scarcity of lithium resources, fiercely drives the development of rechargeable battery systems beyond lithium ion batteries.[1–4] In this regard, rechargeable aluminum batteries are promising candidates with high energy-to-price ratios because of the naturally abundant aluminum resources, which can potentially reduce the material cost and support multiple energy storage applications.[5,6] Rather than one electron transfer in lithium ion batteries, RABs are based on multivalent ion transfer that endow them with ultrahigh theoretical specific gravimetric and volumetric capacities (2978 mA h $g^{-1}$ and 8034 mA h $cm^{-3}$, respectively).[7,8] More importantly, using metallic Al as the anode, the unexpected safety risk is greatly reduced because of its favorable air stability compared with metal Li.[9]

However, finding suitable host materials is a big challenge because of the extremely high charge density of $Al^{3+}$ that greatly reduces the ionic diffusion and solvation-desolvation process, leading to slow diffusion kinetics and poor cycling performance.[10] Since the immense potential of graphite electrodes in chloroaluminate ionic liquid electrolyte was reported by Dai's group in 2015,[11] RABs have lately attracted increasing attention. The operating mechanism of graphite-based electrodes is based on the reversible intercalation/de-intercalation of chloroaluminate anions ($[AlCl_4^-]$) into/out of the graphite layers. Unfortunately, because of the limited ability to store large-sized $[AlCl_4^-]$ anions (0.528 nm) in the interlayer space, the specific capacity of graphite-based electrodes is usually <120 mA h $g^{-1}$. In recent years, other kinds of cathode materials of metal sulphides have been developed for building high performance RABs with high capacity. These materials exhibit high initial discharge capacities (300–400 mA h $g^{-1}$) but suffer from poor cycling stability.[12] Nevertheless, the mechanism responsible for the capacity fading of these metal sulphide electrode materials has been rarely explored in detail up to now. In an effort to understand the above-mentioned problems and then to design high performance metal chalcogenide cathodes for RABs, it is essential to obtain an in-depth understanding of both electrochemical conversion and capacity-deterioration mechanisms for this group of electrode materials.

In this paper, the essential deterioration mechanism, induced by the chemical dissolution of both $Co_9S_8$ and the formed active metal cobalt during the charge/discharge process, has been elucidated for the first time. In addition, reducing the particle size of the active components to the nanoscale is an effective way to solve the sluggish ion diffusion during the

*Department of Materials Science, Fudan University, Shanghai 200433, China. E-mail: yuxuebin@fudan.edu.cn*

† Electronic supplementary information (ESI) available. See DOI: 10.1039/d1ta03465k

‡ Long Yao and Shunlong Ju contributed equally to this work.

electrochemical process, especially for RABs. And then, based on the understanding of the capacity-deterioration mechanism of the $Co_9S_8$ electrode, and the DFT calculation results, we designed a 3D MXene wrapped $Co_9S_8$ NP embedded within a porous carbon matrix ($Co_9S_8$ NP@NPC@MXene) foam composite as a new type of RAB cathode material. Accordingly, MXene nanosheets and porous carbon were utilized to hamper the aggregation and excessive growth of $Co_9S_8$ particles by the strong coupling effect and avoid the dissolution of active cobalt species into the electrolyte by chemical adsorption and physical barriers. As a result, the rationally designed RABs enable the delivery of outstanding electrochemical performance, including a high specific capacity beyond 277 mA h $g^{-1}$ at a specific current of 0.1 A $g^{-1}$ after 100 cycles, excellent rate-cycle capability (110 mA h $g^{-1}$ at 1 A $g^{-1}$ after 1000 cycles), and low polarization. More importantly, the newly developed strategy can be expanded to the modification of the $CoSe_2$ electrode, for which the $CoSe_2$@NPC@MXene cathode also exhibits significantly enhanced cycling stability. These results highlight a high-efficiency strategy to construct high performance $Co_9S_8/CoSe_2$ cathodes and open up a potential avenue for the rational design of metal sulphides/selenides for advanced RABs.

## Results and discussion

In order to study the energy storage and capacity-deterioration mechanism of the $Co_9S_8$ electrode, $Co_9S_8$ nanoparticles embedded in a N-doped hollow porous carbon material ($Co_9S_8$ NP@NPC) was successfully synthesized through heat treatment of ZIF-67 and an appropriate amount of sulfur powder. The XRD pattern of ZIF-67 (Fig. S1†) is in good agreement with previous reports.[13] After annealing, all the peaks of ZIF-67 disappeared, whereas the main peaks attributed to the cubic $Co_9S_8$ crystals and some weak peaks belonging to low graphitic carbon (Fig. S2†) were observed,[14,15] revealing the complete conversion of ZIF-67 to the $Co_9S_8$ NP@NPC composite. The morphology and microstructure were confirmed by scanning electron microscopy (SEM) and transmission electron microscopy (TEM) measurements. According to the SEM image (Fig. 1a), $Co_9S_8$ NP@NPC shows a clear hollow porous structure, which is derived from the Kirkendall effect. Identical to the SEM observation, the TEM image (Fig. 1b) shows a sharp contrast between the interior cavities and edges of the shell, also demonstrating its hollow structure. The high-resolution TEM (HRTEM) observation (Fig. 1c) indicates that the $Co_9S_8$ nanoparticles with a particle size of approximately 10 nm are evenly embedded in the carbon matrix, and the lattice fringe spacing of 0.31 nm is attributed to the (311) lattice plane of the cubic $Co_9S_8$ phase. Next, a Swagelok-type cell was assembled using high-purity aluminum as the counter electrode to test the electrochemical properties of the $Co_9S_8$ NP@NPC electrode. Fig. 1d displays the galvanostatic charge–discharge (GCD) curves of $Co_9S_8$ NP@NPC at the 1st, 40th, 60th and 100th cycles at a current density of 0.1 A $g^{-1}$. $Co_9S_8$ NP@NPC shows a high initial discharge capacity of 220 mA h $g^{-1}$; however, the platform becomes less obvious as the number of cycles increases. After 100 cycles, the capacity decreased rapidly to 40 mA h $g^{-1}$. Obviously, $Co_9S_8$ NP@NPC exhibits a fast capacity degradation.

For thoroughly understanding the aluminum-storage mechanism of $Co_9S_8$, the valence change of the electrode materials at various electrochemical states was observed by the XPS technique. It is clear that after discharge, the spectrum of Co $2p_{3/2}$ shifts to a low binding energy area and two new peaks ($Co^0$ $2p_{3/2}$ at 777.4 eV and $Co^0$ $2p_{1/2}$ at 792.6 eV) are observed (Fig. 1e), which indicates the presence of metallic Co (zero valence state) in the electrode.[16,17] In addition, the intensity of the Al 2p peak (Fig. S3†) is stronger in the fully discharged state than that of the fully charged state, which is also consistent with the decomposition of aluminum compounds of the charged electrode. This phenomenon may be ascribed to the formation of Co from the insertion of $Al^{3+}$ into the $Co_9S_8$ phase. Moreover, the intensity of the Cl 2p peak does not change significantly in the fully discharged and charged state, indicating that Cl is not involved in the reaction (Fig. S4†). Surprisingly, when the separator, taken out from the fully discharged battery, was immersed in absolute ethanol, a light green color was observed, and the color gradually darkened as the cycle number increased (Fig. 1f, the front row), while no color change was observed for a fresh electrolyte. The same color change was also observed when the $Co_9S_8$ NP@NPC sample was dropped into the fresh electrolyte (Fig. 1f, the second row), which suggests that the $Co_9S_8$ active ingredient from the electrode material is also dissolved in the employed electrolyte. To prove this hypothesis, the concentration of Co species in electrolytes obtained from different cycles was analyzed *via* inductively coupled plasma mass spectrometry (ICP-MS, Fig. 1f). Obviously, the battery electrolyte contains significant amounts of Co species, indicating that the active Co species migrate from the $Co_9S_8$ phase to the electrolyte during electrochemical cycling. On the other hand, the concentration of Co species increased significantly with the increase of the cycle number, showing that the $Co_9S_8$ NP@NPC electrode underwent serious structural pulverization during the long cycling process, which is further confirmed by the serious structural crushing of the $Co_9S_8$ NP@NPC sample after long cycling (Fig. S5†). The possible energy storage mechanism of the $Co_9S_8$ cathode was further supported by the DFT calculations (Fig. 1g). Various reaction pathways were considered, including (I) intercalation of $Al^{3+}$ at the octahedral site in $Co_9S_8$;(II) intercalation of $Al^{3+}$ at the tetrahedral site in $Co_9S_8$; (III) incorporation of $Al^{3+}$ into $Co_9S_8$ to generate metallic Co and $Al_xCo_{9-x}S_8$ (*i.e.*, partial substitution of $Co^{2+}$ by $Al^{3+}$); and (IV) conversion reaction that generates metallic Co and $Al_2S_3$ (*i.e.*, $Co^{2+}$ is completely substituted by $Al^{3+}$). To evaluate the feasibility of every reaction, the formation energy ($E_f$) was calculated as follows,

$$E_f = \sum E_{resultant} - \sum E_{reactant}$$

where $E_{resultant}$ and $E_{reactant}$ are the total energy of the reaction product and reactant in a certain reaction, respectively. A reaction with negative $E_f$ was favorable to occur thermodynamically, while a positive $E_f$ suggested that this reaction was difficult to perform. As illustrated in Fig. 1g, only reaction (IV)

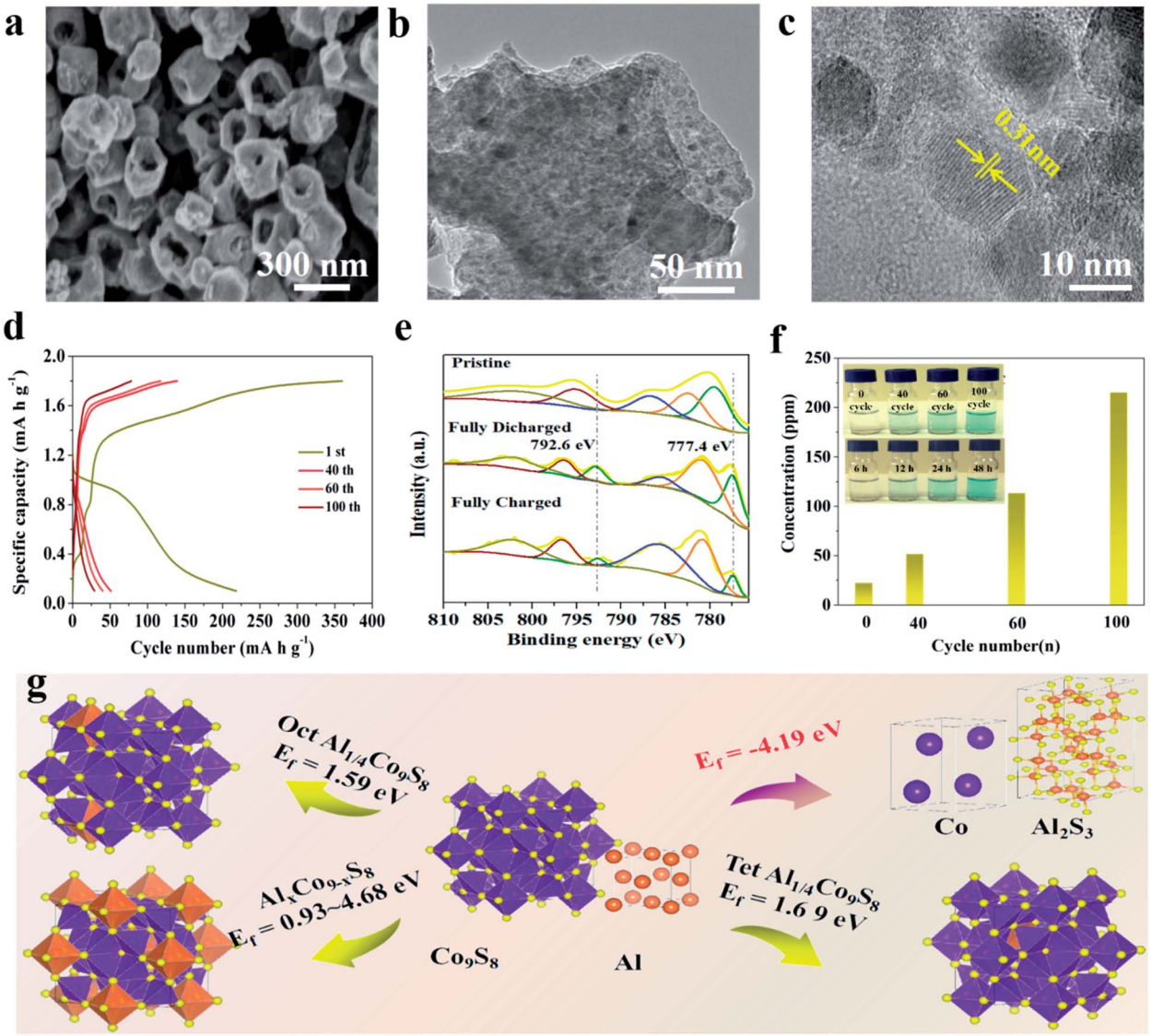


Fig. 1 The electrochemical mechanism of $Co_9S_8$ NP@NPC. (a) SEM, (b) TEM and (c) HRTEM images; (d) The 1st, 40th, 60th and 100th GCD curves at 0.1 A $g^{-1}$; (e) XPS signals of Co 2p at various electrochemical states for the $Co_9S_8$ NP@NPC electrode; (f) the concentrations of the Co element in the electrolyte after different cycles. The inset shows the photos of the electrolyte of a battery containing the $Co_9S_8$ NP@NPC cathode after 0 cycle, 40 cycles, 60 cycles and 100 cycles, respectively (front row), and photos of ethanol solutions of electrolyte with dissolved $Co_9S_8$ NP@NPC after 6 h, 12 h, 24 h and 48 h, respectively (second row); (g) illustration of the energy storage mechanism calculated using DFT.

had a negative $E_f$ of −4.19 eV, indicating the preferential formation of Co metal and $Al_2S_3$ during the discharge processes (*i.e.*, $Co^{2+}$ is completely substituted by $Al^{3+}$). Accordingly, there are three critical processes that substantially impact the electrochemical performance of $Co_9S_8$: (I) a gradual dissolution of the $Co_9S_8$ phase and migration of Co species from the electrode to the electrolyte, resulting in a rapid aluminization-related redox process, along with the loss of the active phase and irreversible capacity decay; (II) a pulverization of $Co_9S_8$ NP@NPC upon repeated cycling, leading to the electrode with worse conductivity; (III) the nature of the high charge density of $Al^{3+}$ leads to a strong bonding between $Al^{3+}$ ions and cathode materials that results in slow diffusion kinetics. To solve these issues, it is desired to design a host material that can accommodate the active material to inhibit its excessive dissolution and pulverization, as well as enhance the ion diffusion kinetics during electrochemical reactions.

MXenes, a rapidly growing type of two-dimensional (2D) material, combining hydrophilic surface, controllable flexible interlayer spacing, superb intercalation effect, high metallic conductivity and rich surface functional groups, have shown promising ion intercalation properties and kinetics in electrochemical applications.[18–20] Our DFT calculation results show that both the pristine MXene and MXene with oxygen surface functional groups are promising materials for the efficient adsorption of cobalt species. As indicated in Fig. 2a–c, the binding energies ($E_b$) between $Ti_3C_2$, $Ti_3C_2$–O, $Ti_3C_2$–OH and soluble Co species were estimated to be −6.63, −4.57, and

 

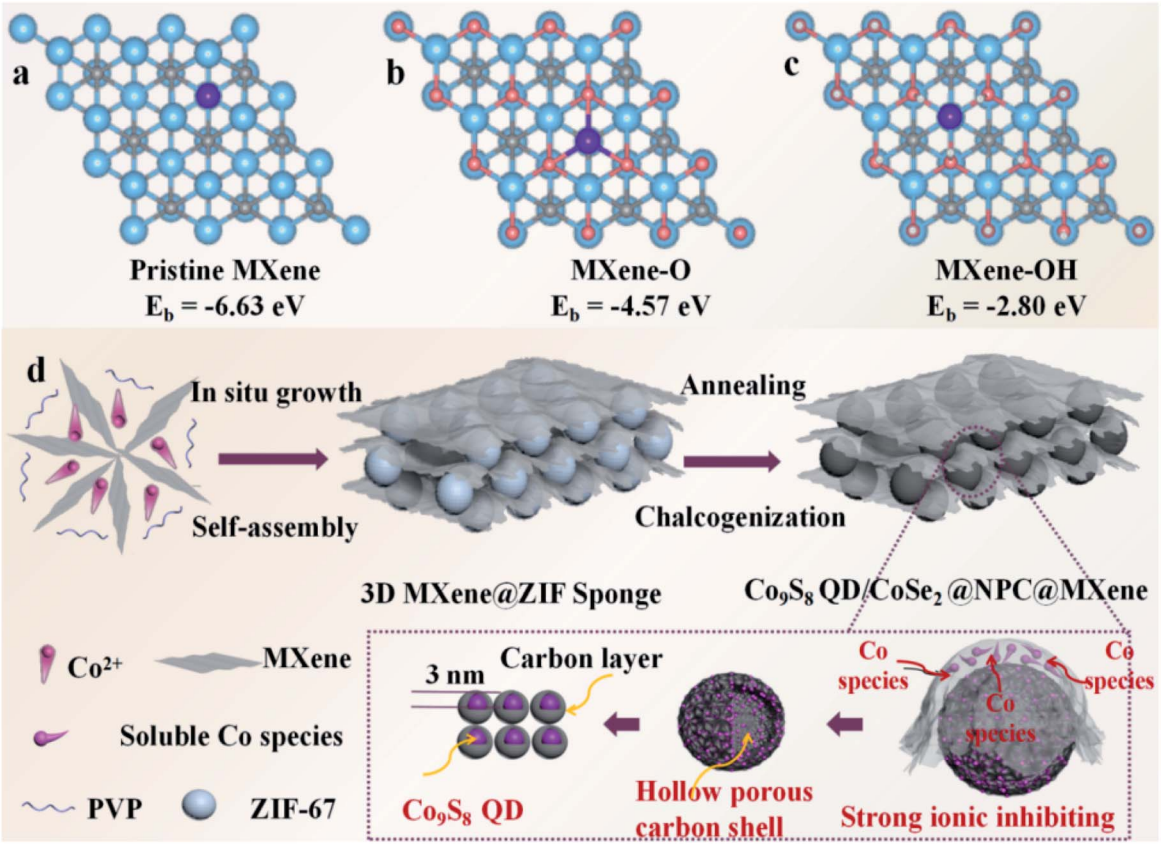


Fig. 2 (a–c) The binding energies of $Ti_3C_2$–Co and $Ti_3C_2$–O–Co calculated using DFT. (d) Schematic illustration of the synthetic process of $Co_9S_8$ NP@NPC@MXene.

−2.80 eV, respectively. Projected density of states (PDOS) and charge density difference plots were employed to further analyze the binding effect. As shown in Fig. S6(a and b),† charge redistribution occurs on the surface after Co adsorption. And as illustrated in Fig. S6(c and d),† the state of Co overlaps that of $Ti_3C_2$ or $Ti_3C_2$–O in the valence band. These results confirm covalent hybridization interactions between Co and the substrate. This suggests that both the pristine MXene and MXene with oxygen-containing functional groups exhibit a considerable binding effect towards the soluble Co species, thus achieving potential inhibition performance. In addition, reducing the particle size is an effective way to solve the sluggish ion diffusion.[21,22] Accordingly, for inhibiting the unexpected shuttle effects induced by chemical dissolution and improving the diffusion kinetics of the $Co_9S_8$ positive electrode, the MXene and hollow N-doped porous carbon nanobox dual-confined $Co_9S_8$ nanoparticles ($Co_9S_8$ NP@NPC@MXene) were particularly designed to achieve excellent Al-storage capability, as shown in Fig. 2d. First, with the help of PVP as a bridge, Co-ions were firmly adsorbed on the surface of the MXene and embedded in PVP resin. Afterward, 3D ZIF-67@MXene sponge-like precursors are prepared through the coordination of $Co^{2+}$ with 2-methylimidazole, followed by freeze-drying. Finally, the $Co_9S_8$ NP@NPC@MXene sponge-like composite can be synthesized through one-step carbonization and vulcanization.

The MXene and carbon-confined hollow structure with strong chemical coupling not only maintain the structural stability but also effectively hamper the aggregation and excessive growth of $Co_9S_8$ particles and avoid the loss of active cobalt species into the electrolyte by chemical adsorption and physical barriers. Inspired by these merits, the systematic study of the resultant materials was carried out. The SEM image in Fig. 3a shows the modified ZIF-67 coated with a thin layer of flexible MXene, forming a three-dimensional interconnected conductive network. The enlarged SEM image (Fig. 3b) further shows that the thin MXene layer for interfacial assembly uniformly covers on the surface of the dispersed ZIF-67 crystals with a wrinkled surface. In comparison, MXene sheets (Fig. S7†) have a thick flake-like shape with a flat and smooth surface that results from the agglomeration caused by van der Waals interactions. The microstructure of the resultant $Co_9S_8$ NP@NPC@MXene composite was further characterized by SEM and TEM (Fig. 3c and d), respectively, where the uniform hollow carbon nanoboxes are well distributed on the MXene. The magnified TEM image shows that these nanoboxes with numerous particles and a continuous carbon shell inherited well the shape of the Co-ZIFs precursor, where the thickness of the carbon shell is about 10 nm (Fig. 3e). This special hollow structure not only significantly facilitates a fast electron transport and reduces the ion diffusion distance but also efficiently

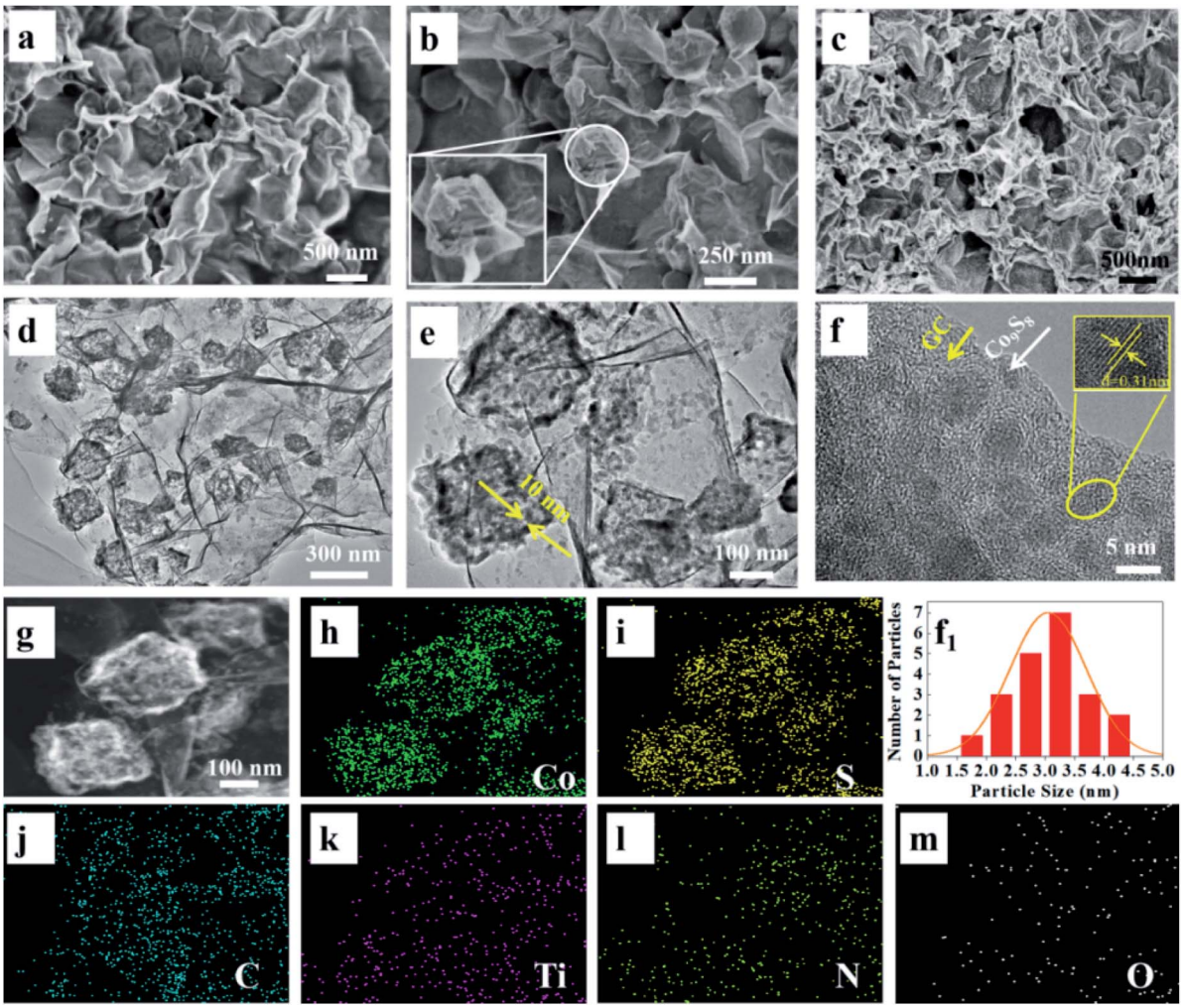


Fig. 3 Morphology of ZIF-67@MXene and $Co_9S_8$ NP@NPC@MXene. SEM images of the (a and b) ZIF-67@MXene precursor and (c) $Co_9S_8$ NP@NPC@MXene; (d and e) TEM image of $Co_9S_8$ NP@NPC@MXene; (f) HRTEM image of $Co_9S_8$ NP@NPC@MXene (inset shows the HRTEM image of $Co_9S_8$) and the corresponding ($f_1$) particle size distribution; (g) HAADF-STEM image of $Co_9S_8$ NP@NPC@MXene and the corresponding elemental mapping images (h–m).

accommodates a large volume expansion of the $Co_9S_8$ active substance during repeated discharge/charge processes.[23–25] The HRTEM image of $Co_9S_8$ NP@NPC@MXene (Fig. 3f) and the corresponding particle size distribution (Fig. 3$f_1$) clearly show that the $Co_9S_8$ nanocrystals with a particle size of approximately 3 nm are evenly embedded in the carbon framework, and greatly decreased compared with the $Co_9S_8$ particles in $Co_9S_8$ NP@NPC (Fig. 1c). This implies that the introduction of the MXene and the converted carbon matrix acts as a "double-confined nanospace", effectively inhibiting the growth of $Co_9S_8$ nanocrystals. The construction of nanoarchitectures would be helpful to increase the active sites and shorten the ion diffusion distance, thus boosting the reaction kinetics, especially for Al batteries.[22] Furthermore, the high-angle annular dark-field scanning TEM (HAADF-STEM) image of $Co_9S_8$ NP@NPC@MXene shows a homogeneous dispersion of bright dots within the polyhedral frame and confirms that the $Co_9S_8$ NPs are uniformly embedded in the hollow porous carbon nanobox (Fig. 3g). The elemental mapping images further reflected the presence and the uniform distribution of Co, S, C, Ti, N and O elements within the interconnected conductive network (Fig. 3h–m).

The X-ray diffraction (XRD) patterns (Fig. 4a and S8†) show that the coexistence of ZIF-67 and MXene can be observed for the as prepared ZIF-67@MXene precursor.[26,27] After carbonization and sulfidation, the ZIF-67@MXene was completely converted into the $Co_9S_8$ NP@NPC@MXene composite. Notably, the corresponding $Co_9S_8$ diffraction peaks exhibit line broadening due to the ultrafine crystallite size of the obtained $Co_9S_8$ particles, which agrees well with the HRTEM observations. To further analyze the porous structure and textural properties of the $Co_9S_8$ NP@NPC@MXene composite, $N_2$ adsorption–desorption isotherms were recorded. As can be seen from Fig. 4b, the $Co_9S_8$ NP@NPC@MXene composite exhibits a typical type IV isotherm with a hysteresis loop at $p/p_0 = 0.4$–0.8, implying the abundant existence of mesopores.[28] The corresponding pore size distribution curve (Fig. 4c) shows abundant mesopores of the resultant material in the range of 2–10 nm. The Brunauer–Emmett–Teller (BET) specific surface area

 

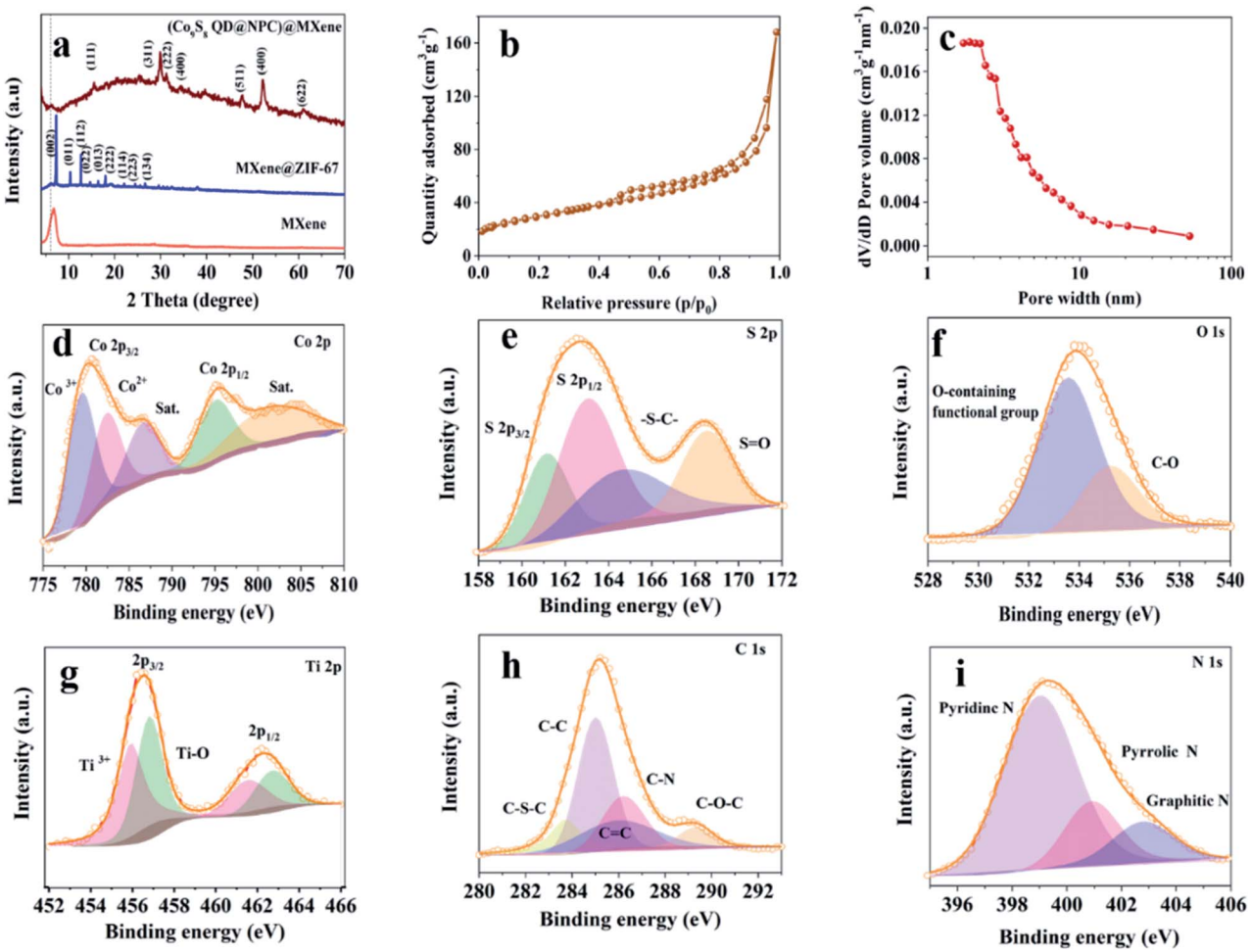


Fig. 4 Physical chemical properties of the as-prepared samples. (a) XRD patterns of MXene, ZIF-67@MXene and $Co_9S_8$ NP@NPC@MXene; (b) $N_2$ adsorption/desorption isotherm of $Co_9S_8$ NP@NPC@MXene and (c) the corresponding pore size distribution; High-resolution XPS spectra of (d) Co 2p, (e) S 2p, (f) O 1s, (g) Ti 2p, (h) C 1s and (i) N 1s for $Co_9S_8$ NP@NPC@MXene.

of the $Co_9S_8$ NP@NPC@MXene was estimated to be 107 $m^2\ g^{-1}$. Such a favorable BET surface area with a suitable pore size distribution may be beneficial for enhancing the ion transport and buffering the volume change of the $Co_9S_8$ NPs during repeated cycling.[28] The X-ray photoelectron spectroscopy (XPS) survey spectra further confirmed the coexistence of Co, S, C, Ti, O and N elements in the $Co_9S_8$ NP@NPC@ MXene sample. The high resolution Co 2p spectrum (Fig. 4d) shows the existence of $Co^{2+}$ and $Co^{3+}$, suggesting the formation of $Co_9S_8$ in the carbon structure.[29] According to the S 2p spectrum (Fig. 4e), the presence of S $2p_{2/3}$ and S $2p_{1/3}$ peaks further suggests that $Co_9S_8$ is successfully synthesized.[30] Meanwhile, the existence of the C–S–C and S═O bonds might be attributed to the coupling effect between the $Co_9S_8$ phase and carbon, as well as the residual hydroxide groups in the MXene (Fig. 4f). In comparison, there is no characteristic peak with S═O in the S 2p spectrum of $Co_9S_8$ NP@NPC without the MXene coating (Fig. S9†). The Ti 2p spectrum (Fig. 4g) shows the peaks of the $Ti^{3+}$ and Ti–O bonds, which is in accordance with previously reported studies.[20,31] Fig. 4h shows the high-resolution C 1s spectrum that has been deconvoluted into five peaks, corresponding to C–S–C (283.5 eV), C–C (284.5 eV), C═C (285.5 eV), C–O–C (286.5 eV) and C–N (289.5 eV), respectively.[28] The existence of C–N and C–S–C indicate the N element doping into carbon materials and the coupling effect between the carbon materials and $Co_9S_8$ active phase, respectively. As shown in Fig. 4i, the N 1s XPS spectrum shows that the nitrogen species exist in the form of graphitic, pyridinic, and pyrrolic structures.[32] The pyridinic N can directly couple with graphite carbon and metal atoms, and the pyrrolic N helps to induce defects and active sites, which is beneficial for the improvement of electrochemical performance by promoting $Al^{3+}$ diffusion. The above results indicate that there is a chemical interaction between the $Co_9S_8$ phase, $Ti_3C_2$ MXene and carbon layer. Compared with weak physical effects, such a strong chemical coupling may significantly improve the structural stability and enhance the charge transfer kinetics, which is essential to inhibit the dissolution and migration of active cobalt species from electrode materials to the electrolyte during the electrochemical processes. According to Fig. S10,† the content of $Co_9S_8$ in the $Co_9S_8$ NP@NPC@MXene sample is about 64.28 wt%.

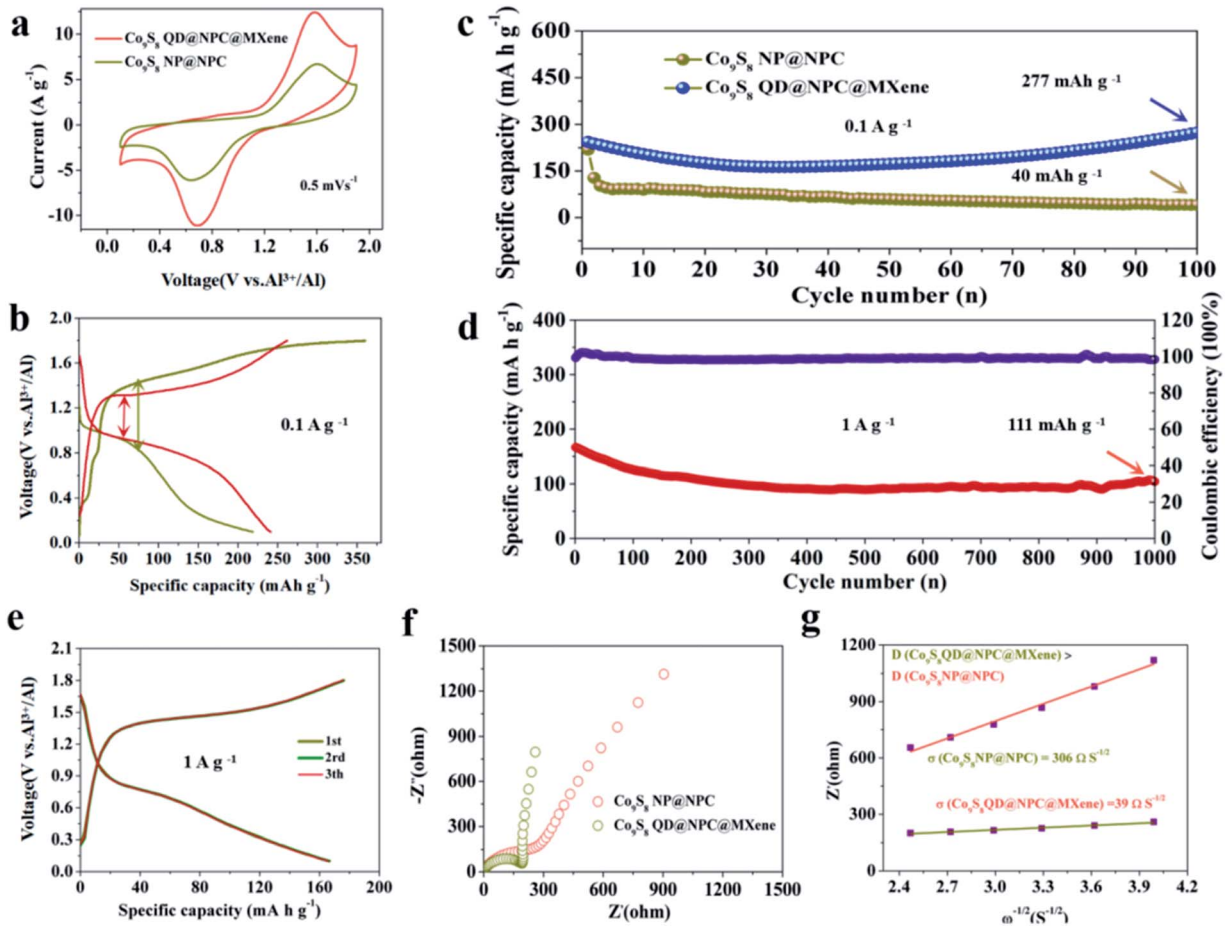


Fig. 5 Electrochemical performance. (a) CV curves of $Co_9S_8$ NP@NPC@MXene and $Co_9S_8$ NP@NPC at 0.5 mV $s^{-1}$; (b) GCD curves of $Co_9S_8$ NP@NPC@MXene and $Co_9S_8$ NP@NPC at 0.1 A $g^{-1}$; (c) Capacity stability of $Co_9S_8$ NP@NPC@MXene and $Co_9S_8$ NP@NPC at 0.1 A $g^{-1}$; (d) the long cycle stability with coulombic efficiency of $Co_9S_8$ NP@NPC@MXene at 1 A $g^{-1}$; (e) the 1st, 2nd, and 3rd charge–discharge curves of $Co_9S_8$ NP@NPC@MXene at 1 A $g^{-1}$; (f) Nyquist plots of $Co_9S_8$ NP@NPC@MXene and $Co_9S_8$ NP@NPC at 0.1 V; (g) the linear relation of $\omega^{-1/2}$ *versus* $Z$.

The electrochemical behavior of the $Co_9S_8$ NP@NPC@MXene, $Co_9S_8$ NP@NPC and pure $Co_9S_8$ cathodes is shown in Fig. 5 and S11.† At a scanning rate of 0.5 mV $s^{-1}$, the typical CV curves of the two samples show a pronounced pair of redox peaks,[16] indicating analogous electrochemical behaviors (Fig. 5a). Obviously, $Co_9S_8$ NP@NPC@MXene has a larger curve area and higher redox peak current than $Co_9S_8$ NP@NPC, indicating that $Co_9S_8$ NP@NPC@MXene has a larger capacity and faster ion insertion/extraction kinetics. Compared to the $Co_9S_8$ NP@NPC@MXene cathode material, the simple $Co_9S_8$ NP@NPC clearly shows a negative shift in the cathodic peaks and positive shift in the anodic peaks, which should be attributed to the electrode polarization during cycling because of the sluggish redox kinetics.[33] As shown in Fig. 5b, the GCD curves at 0.1 A $g^{-1}$ show that $Co_9S_8$ NP@NPC@MXene presents a longer voltage plateau and lower polarization, with a higher specific discharge capacity of 241 mA h $g^{-1}$, indicating that more amount of the $Co_9S_8$ active material is involved in the reaction. Moreover, both the charge and discharge voltage plateaus are consistent with the CV measurements. As shown in Fig. 5c, a typical discharge capacity of 277 mA h $g^{-1}$ is well preserved after 100 cycles at 0.1 A $g^{-1}$. The increase of capacity during the cycling process may be due to the activation step, which has also been observed in previous reports.[34] For comparison, a bare $Co_9S_8$ sample was synthesized through a similar vulcanization process except using commercial Co powder as the precursor. The crystallinity of the bare $Co_9S_8$ sample is better than that of $Co_9S_8$ NP@NPC and $Co_9S_8$ NP@NPC@MXene, and there are no impurity phases, as apparent from Fig. S11a.† It is interesting to note that the bare $Co_9S_8$ cathode showed a weak charging and discharging platform and a low initial capacity of 38 mA h $g^{-1}$ (Fig. S11a†). These results indicate that the crystal size of $Co_9S_8$ particles in the $Co_9S_8$ NP@NPC@MXene sample plays a critical role in improving the reactivity of $Co_9S_8$ with Al ions. Along with the GCD curves and the specific capacity of MXene and carbon matrix positive electrodes (Fig. S12 and S13†), it is confirmed that its contribution to the overall electrode capacity is very limited. More encouragingly, $Co_9S_8$ NP@NPC@MXene also contributes to an excellent long-term cycling stability at a high current density of 1 A $g^{-1}$ (Fig. 5d), exhibiting a reversible capacity of 110 mA h $g^{-1}$ after 1000 cycles with a coulombic efficiency over 98%, which outperforms $Co_9S_8$ NP@NPC and

 

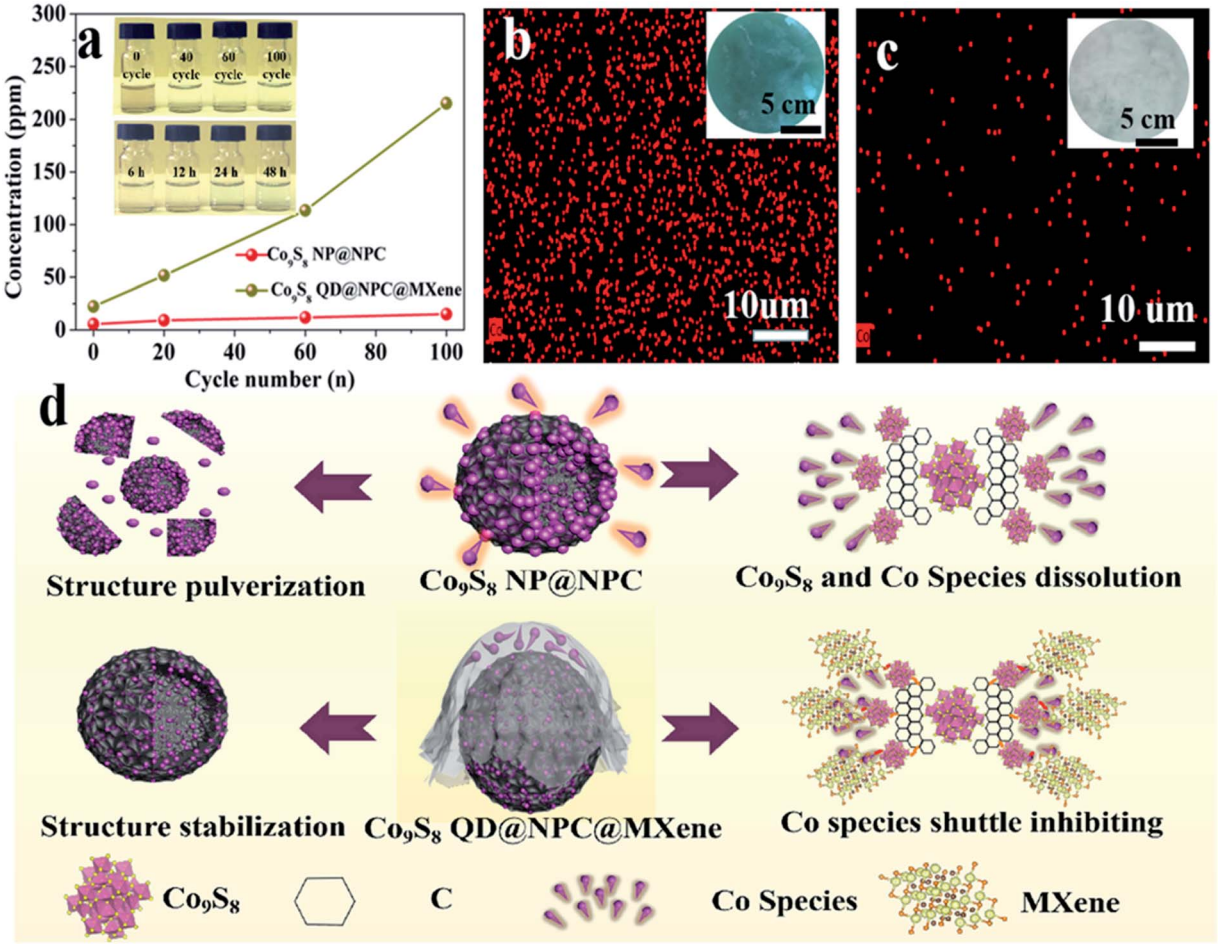


Fig. 6 Mechanism analysis of performance enhancement. (a) The concentrations of the Co element in the electrolyte of the battery containing the $Co_9S_8$ NP@NPC@MXene cathode at different cycles as compared with that of the $Co_9S_8$ NP@NPC cathode. The inset shows the photos of ethanol solutions with the electrolyte of the RABs containing the $Co_9S_8$ NP@NPC@MXene cathode after 0 cycle, 40 cycles, 60 cycles and 100 cycles, respectively (the front row), and electrolyte with dissolved $Co_9S_8$ NP@NPC@MXene after 6 h, 12 h, 24 h and 48 h, respectively (the second row); (b) The Co elemental mapping of the battery separator disassembled from the cell containing the $Co_9S_8$ NP@NPC cathode and (c) $Co_9S_8$ NP@NPC@MXene cathode after being fully discharged, and the corresponding photos of the separator, respectively; (d) The schematic of the performance enhancement of the $Co_9S_8$ NP@NPC@MXene cathode.

pure $Co_9S_8$. Fig. 5e shows the GCD profiles of the $Co_9S_8$ NP@NPC@MXene cathode at the 1st, 2nd, and 3rd cycles at 1 A $g^{-1}$. No obvious change of the voltage plateaus is observed, corresponding to the low polarization, which further confirmed the fast reaction kinetics and high electrochemical reversibility of the $Co_9S_8$ NP@NPC@MXene electrode. The electrochemical impedance spectroscopy (Fig. 5f) results show that the charge-transfer resistance of the $Co_9S_8$ NP@NPC@MXene electrode is much smaller than that of the $Co_9S_8$ NP@NPC electrode, endowing it with faster electrochemical kinetics and thus lower polarization and enhanced rate performance. In order to further investigate the ion diffusion kinetics of the $Co_9S_8$ NP@NPC@MXene cathode, the CV curves at different scan rates from 0.5 to 8 mV $s^{-1}$ were recorded (Fig. S14a†). The linear relation between the measured $v$ (scan rate) and $i$ (current) is according to the equation:

$$i = av^b$$

where both $a$ and $b$ are variable positive numbers, and the $b$ value could be calculated from the slope of plots of $\log(i)$ *versus* $\log(v)$, in which the $b$ value close to 0.5 reflects a diffusion controlled process, while $b$ close to 1.0 corresponds to a surface pseudocapacitive dominated reaction.[35] The fitted slope $b$ values are determined to be 0.78 (peak A) and 0.86 (peak B) (Fig. S14b†), respectively, suggesting that the obtained capacity of the as-prepared $Co_9S_8$ NP@NPC@MXene is mainly dominated by the diffusion reaction. The ratio between these two aspects at various scan rates can be quantitatively determined using the following equation,

$$i_{(V)} = k_1 + k_2 v^{1/2}$$

where $k_1 v$ represents the pseudocapacitive contributions. It was found that the capacitive contribution accounted for 77% of the overall capacity of the $Co_9S_8$ NP@NPC@MXene electrode at 5 mV $s^{-1}$ (Fig. S14c†). Specifically, the pseudocapacitive

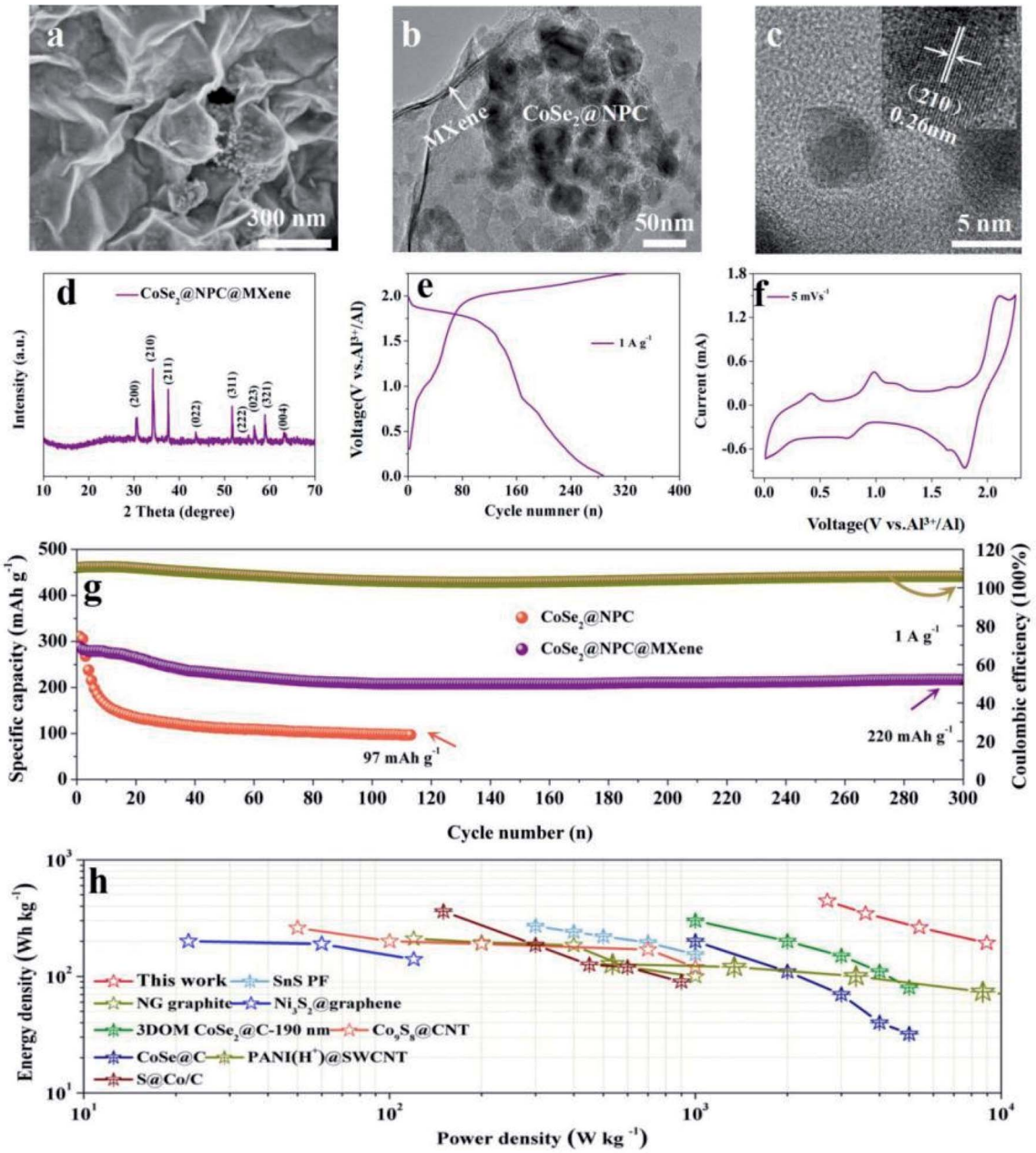


Fig. 7 (a) SEM images of $CoSe_2$@NPC@MXene; (b and c) TEM images of $CoSe_2$@NPC@MXene at different magnifications; (d) XRD patterns of $CoSe_2$@NPC@MXene; (e) GCD curve of $CoSe_2$@NPC@MXene at 1 A $g^{-1}$; (f) CV curve of $CoSe_2$@NPC@MXene at 5 mV $s^{-1}$; (g) capacity stability of $CoSe_2$@NPC@MXene and $CoSe_2$@NPC at 1 A $g^{-1}$; (h) performance comparison of the cells. Note that the specific capacities refer to the composite materials.

contributions were 68%, 73%, 75.0%, and 87% at scan rates of 0.5, 1, 2 and 8 mV $s^{-1}$, respectively (Fig. S14d†), indicating that the pseudocapacitive storage mechanism dominated in the $Co_9S_8$ NP@NPC@MXene electrode at high scan rates. On the other hand, to compare the chemical diffusion kinetics of $Co_9S_8$ NP@NPC@MXene and $Co_9S_8$ NP@NPC samples, the slope of $Z'/\omega^{-1/2}$ curves (Warburg coefficient) was calculated using the following equation:

$$\omega = 2\pi f$$

$$Z_{re} = R + \sigma\omega^{-1/2}$$

$$D = 0.5R^2T^2/A^2n^4F^4C^2\sigma^2$$

where $R$, $T$, $A$, $F$, $n$, $C$, $\sigma$, and $D$ are the gas constant, temperature in Kelvin, the area of electrodes, Faraday constant, number of electrons transferred in a reaction, the molar concentration of $Al^{3+}$, the Warburg coefficient, and the diffusion coefficient, respectively. As shown in the equation, the slopes of $Z'/\omega^{-1/2}$ curves have a positive correlation with $D$. As shown in Fig. 5g, the slope of $Co_9S_8$ NP@NPC@MXene can be calculated to be 39,

 

which is greater than the 306 of $Co_9S_8$ NP@NPC, revealing that $Co_9S_8$ NP@NPC@MXene has an improved $Al^{3+}$ diffusion kinetics. As shown in the first row of Fig. 6a, when the separator, removed from a discharged RAB battery after various cycles, was immersed in absolute ethanol, the color of the electrolyte did not change significantly. Furthermore, no obvious light green colour was observed for the $Co_9S_8$ NP@NPC@MXene sample after immersion in fresh electrolyte from 6 h to 48 h (Fig. 6a, the second row). Meanwhile, the Co species concentration in the electrolyte was determined to be only 5.6 ppm for the $Co_9S_8$ NP@NPC@MXene cathode after 100 cycles, which is dramatically lower than that of the $Co_9S_8$ NP@NPC sample (Fig. 6a), revealing that the presence of MXene effectively inhibited the dissolution and shuttle of cobalt species. Furthermore, according to the EDS mapping of the Co element in the battery separator (Fig. 6b, c and S15†), the intensity of the Co signals of the $Co_9S_8$ NP@NPC@MXene cathode after 100 cycles is significantly weaker than that of the $Co_9S_8$ NP@NPC cathode, indicating again that less $Co_9S_8$ dissolves in the electrolyte of the $Co_9S_8$ NP@NPC@MXene cathode upon cycling. In addition, compared with the green surface of the separator from the cell containing the $Co_9S_8$ NP@NPC cathode formed by ion migration (inset in Fig. 6c), the surface of the separator from the cell containing the $Co_9S_8$ NP@NPC@MXene cathode is much cleaner (inset in Fig. 6d), which further verifies the above experimental results. As observed in the postmortem study, the morphology and structural integrity of the $Co_9S_8$ NP@NPC@MXene hybrids (Fig. S16†) are well maintained after 100 cycles at 0.1 A $g^{-1}$, confirming that the MXene layer can effectively prevent the pulverization of $Co_9S_8$ NP@NPC. Finally, as illustrated in Fig. 6d, through our design, multiple merits for enhancing the electrochemical performance are simultaneously achieved in the $Co_9S_8$ NP@NPC@MXene cathode: (I) the MXene and carbon-confined hollow structure with strong chemical coupling not only improve the reaction kinetics but also effectively suppress the dissolution of $Co_9S_8$ and avoid the loss of active cobalt species; (II) ultrafine $Co_9S_8$ quantum dots are conducive to the diffusion kinetics and mitigating volume expansion, thus greatly enhancing the electrochemical reactivity; (III) the good 3D diffusion kinetics and mitigating volume expansion greatly enhance the electrochemical reactivity; (III) the good 3D interconnected conductive network with MXenes ensures structural integrity to facilitate electron transfer upon cycling.

To demonstrate the general versatility of our proposed surface engineering strategy, we evaluated the aluminum storage properties of other metal chalcogenides. Similar MXene-wrapped polyhedral structures can be observed from the SEM and TEM images of $CoSe_2$@NPC@MXene composites (Fig. 7a and b). According to the high-resolution TEM (HRTEM) analysis (Fig. 7c), it can be observed that the $CoSe_2$ nanoparticles have a size of 5 nm and a crystal plane spacing of 0.26 nm, which corresponds to the (210) plane of the $CoSe_2$ crystals. As can be seen from Fig. 7d, the diffraction peaks located at 30.5, 34.2, 37.6, 51.7, and 58.9° were well indexed to the (200), (210), (211), (311), and (321) planes of standard $CoSe_2$. The typical CV profile shows two reduction peaks at 0.9 and 1.8 V and two oxidation peaks at 1.0 and 2.1 V at a scanning rate of 5 mV $s^{-1}$ (Fig. 7e). According to the GCD curves (Fig. 7f), the reduction peaks located at 0.9 and 1.8 V and corresponding oxidation peaks at 1.0 and 2.0 V were consistent with those of the CV curve. Moreover, $CoSe_2$@NPC@MXene delivered a high discharge capacity of up to 288 mA h $g^{-1}$ at 1 A $g^{-1}$ and maintained a desirable capacity retention of approximately 220 mA h $g^{-1}$ after 300 cycles and 155 mA h $g^{-1}$ after 1000 cycles, while the capacitance of $CoSe_2$@NPC suffered from rapid degradation (Fig. 7g and S17†), which exhibited an improved rechargeability by introduction of MXene to prevent the loss of active Co species. As shown in Fig. S18 and Table S1,† the excellent rate-cycling stabilities of RABs based on the $Co_9S_8$ NP@NPC@MXene electrode and $CoSe_2$@NPC@MXene electrode are superior to those of most previously reported cathodes, which is ascribed to the fast diffusion kinetics and structural stability. Moreover, the reversible capacities of $CoSe_2$–NPCS are 230.8, 160.5, 128.9 and 114.0 mA h $g^{-1}$ at stepwise current densities of 1.5, 2, 3 and 5.0 A $g^{-1}$, respectively (Fig. S19†). Finally, Fig. 7h compares the Ragone plots of state-of-the-art Al batteries.[16,36] With the high reversible capacity, high operating voltage and superior diffusion dynamics, the $CoSe_2$@NPC@MXene cathode material demonstrates a specific energy of 446 W h $kg^{-1}$, while still providing a high specific power of 2700 W $kg^{-1}$, making it potentially competitive against other conventional electrochemical energy storage devices.

## Conclusion

In summary, a universal and effective surface engineering strategy has been explored to construct 3D MXene-wrapped cobalt sulfides/selenides embedded within a hollow carbon nanobox, which forms a 0D–2D–3D multi-dimensional architecture for tackling the unexpected capacity decay induced by the loss of soluble active cobalt species. The strongly coupled MXene and N-doped hollow carbon dual-confinement strategy not only hampers the aggregation and excessive growth of particles but also effectively suppresses the shuttle effect caused by the soluble cobalt species in the electrolyte. As a consequence, the resulting representative metal $Co_9S_8$ and $CoSe_2$ electrodes exhibit an outstanding reversible capacity and long-term cycling stability, even at high current density. This elaborate work would be of great significance for the further development of advanced metal chalcogenides for RAB cathodes with excellent electrochemical performances.

## Conflicts of interest

The authors declare that they have no competing interests.

## Acknowledgements

This work was partially supported by the National Key Research and Development Program of China (2017YFA0204600), the National Science Fund for Distinguished Young Scholars (51625102), the National Natural Science Foundation of China

(51971065), and the Innovation Program of Shanghai Municipal Education Commission (2019-01-07-00-07-E00028).

## References

1 J. Gao, G. Wang, Y. Liu, J. Li, B. Peng, S. Jiao, S. Zeng and G. Zhang, *J. Mater. Chem. A*, 2020, **8**, 13946.
2 H. Yang, L. W. Chen, F. He, J. Zhang, Y. L. Zhao, B. Wang, L. He and Y. Yu, *Nano Lett.*, 2020, **20**, 758.
3 X. Zhang, L. Li, E. Fan, Q. Xue, Y. Bian, F. Wu and R. Chen, *Chem. Soc. Rev.*, 2018, **47**, 7239.
4 B. Li, Y. Liu, X. Jin, S. Jiao, G. Wang, B. Peng, S. Zeng, L. Shi, J. Li and G. Zhang, *Small*, 2019, **15**, 1902881.
5 Z. Liu, J. Wang, X. Jia, W. Li, Q. Zhang, L. Fan, H. Ding, H. Yang, X. Yu and X. Li, *ACS Nano*, 2019, **13**, 10631.
6 J. Xie and Q. Zhang, *Small*, 2019, **15**, 1805061.
7 H. Yang, H. Li, J. Li, Z. Sun, K. He, H. Cheng and F. Li, *Angew. Chem., Int. Ed.*, 2019, **58**, 11978.
8 Z. Zhao, Z. Hua, Q. Li, H. Li, X. Zhang, Y. Zhuang, F. Wang and G. Yu, *Nano Today*, 2020, **32**, 100870.
9 X. Zhang, S. Jiao, J. Tu, W. L. Song, X. Xiao, S. Li, M. Wang, H. Lei, D. Tian, H. Chen and D. Fang, *Energy Environ. Sci.*, 2019, **12**, 1918.
10 Z. A. Zafar, S. Imtiaz, R. Razaq, S. Ji, T. Huang, Z. Zhang, Y. Huang and J. A. Anderson, *J. Mater. Chem. A*, 2017, **5**, 5646.
11 M. C. Lin, M. Gong, B. Lu, Y. Wu, D. Y. Wang, M. Guan, M. Angell, C. Chen, J. Yang, B. J. Hwang and H. Dai, *Nature*, 2015, **520**, 325.
12 (*a*) H. Li, H. Yang, Z. Sun, Y. Shi, H. M. Cheng and F. Li, *Nano Energy*, 2019, **56**, 100; (*b*) S. Wang, Z. Yu, J. Tu, J. Wang, D. Tian, Y. Liu and S. Jiao, *Adv. Energy Mater.*, 2016, **13**, 1600137; (*c*) S. Wang, S. Jiao, J. Wang, H. S. Chen, D. Tian, H. Lei and D. N. Fang, *ACS Nano*, 2017, **11**, 469; (*d*) Z. Hu, K. Zhi, Q. Li, Z. Zhao, H. Liang, X. Liu, J. Huang, C. Zhang, H. Li and X. Guo, *J. Power Sources*, 2019, **440**, 227147; (*e*) R. Zhuang, Z. Huang, S. Wang, J. Qiao, J. C. Wu and Ji. Yang, *Chem. Eng. J.*, 2021, **409**, 128235.
13 H. Hu, J. Zhang, B. Guan and X. W. Lou, *Angew. Chem., Int. Ed.*, 2016, **55**, 9514.
14 W. Peng, Y. Wang, X. Yang, L. Mao, J. Jin, S. Yang, K. Fu and G. Li, *Appl. Catal., B*, 2020, **268**, 118437.
15 J. Liu, C. Wu, D. Xiao, P. Kopold, L. Gu, P. A. Aken, J. Maier and Y. Yu, *Small*, 2016, **12**, 2354.
16 Y. Hu, D. Ye, B. Luo, H. Hu, X. Zhu, S. Wang, L. Li, S. Peng and L. Wang, *Adv. Mater.*, 2018, **30**, 1703824.
17 T. Cai, L. Zhao, H. Hu, T. Li, X. Li, S. Guo, Y. Li, Q. Xue, W. Xing, Z. Yan and L. Wang, *Energy Environ. Sci.*, 2018, **11**, 2341.
18 Y. Deng, T. Shang, Z. Wu, Y. Tao, C. Luo, J. Liang, D. Han, R. Lyu, C. Qi, F. Kang and Q. H. Yang, *Adv. Mater.*, 2019, 1902432.
19 R. Zhao, H. Di, X. Hui, D. Zhao, R. Wang, C. Wang and L. Yin, *Energy Environ. Sci.*, 2020, **13**, 246.
20 Y. T. Liu, P. Zhang, N. Sun, B. Anasori, Q. Z. Zhu, H. Liu, Y. Gogotsi and B. Xu, *Adv. Mater.*, 2018, **30**, 17073349.
21 S. J. Yang, S. Nam, T. Kim, J. H. Im, H. Jung, J. H. Kang, S. Wi, B. Wi and C. R. Park, *J. Am. Chem. Soc.*, 2013, **135**, 7394.
22 T. Mori, Y. Orikasa, K. Nakanishi, C. Kezheng, M. Hattori, T. Ohta and Y. J. Uchimoto, *J. Power Sources*, 2016, **313**, 9.
23 R. Wu, X. Qian, K. Zhou, J. Wei, J. Lou and P. M. Ajayan, *ACS Nano*, 2014, **8**, 6297.
24 T. Yoon, T. Bok, C. Kim, Y. Na, S. Park and K. S. Kim, *ACS Nano*, 2017, **11**, 4808.
25 W. Mao, W. Yue, Z. Xu, S. Chang, Q. Hu, F. Pei, X. Huang, J. Zhang, D. Li, G. Liu and G. Ai, *ACS Nano*, 2020, **14**, 4741.
26 Y. Zhu, K. Rajoua, S. L. Vot, O. Fontaine, P. Simon and F. Favier, *Nano Energy*, 2020, **73**, 104734.
27 Y. Zhou, D. Yan, H. Xu, J. Feng, X. Jiang, J. Yue, J. Yang and Y. Qian, *Nano Energy*, 2015, **12**, 528.
28 Z. Chen, R. Wu, M. Liu, H. Wang, H. Xu, Y. Guo, Y. Song, F. Fang, X. Yu and D. Sun, *Adv. Funct. Mater.*, 2017, **27**, 1702046.
29 S. Dou, L. Tao, J. Huo, S. Wang and L. Dai, *Energy Environ. Sci.*, 2016, **9**, 1320.
30 J. Zhong, T. Wu, Q. Wu, S. Du, D. Chen, B. Chen, M. Chang, X. Luo and Y. J. Liu, *J. Power Sources*, 2019, **417**, 90.
31 J. Halima, K. M. Cook, M. Naguibe, P. Eklundc, Y. Gogotsi, J. Rosenc and M. W. Barsoum, *Appl. Surf. Sci.*, 2016, **362**, 406.
32 X. Bai, L. Wang and Y. Lin, *Mater. Lett.*, 2020, **264**, 127342.
33 J. Yu, J. Xiao, A. Li, Z. Yang, L. Zeng, Q. Zhang, Y. Zhu and L. Guo, *Angew. Chem., Int. Ed.*, 2020, **59**, 13071.
34 D. J. Yoo, M. Heeney, F. Glöcklhofer and J. W. Choi, *Nat. Commun.*, 2021, **12**, 2386.
35 J. Li, G. Wang, L. Yu, J. Gao, Y. Li, S. Zeng and G. Zhang, *ACS Appl. Mater. Interfaces*, 2021, **13**, 13139.
36 (*a*) K. Liang, L. Ju, S. Koul, A. Kushima and Y. Yang, *Adv. Energy Mater.*, 2018, 1802543; (*b*) D. Y. Wang, C. Y. Wei, M. C. Lin, C. J. Pan, H. L. Chou, H. A. Chen, M. Gong, Y. Wu, C. Yuan and M. Angell, *Nat. Commun.*, 2017, **8**, 14283; (*c*) S. Wang, Z. Yu, J. Tu, J. Wang, D. Tian, Y. Liu and S. Jiao, *Adv. Energy Mater.*, 2016, 1600137; (*d*) H. Hong, J. Liu, H. Huang, C. A. Etogo, X. Yang, B. Guan and L. Zhang, *J. Am. Chem. Soc.*, 2019, **141**, 14764; (*e*) W. Xing, D. Du, T. Cai, X. Li, J. Zhou, Y. Chai, Q. Xue and Z. Yan, *J. Power Sources*, 2018, **401**, 6; (*f*) S. Wang, S. Huang, M. Yao, Y. Zhang and Z. Niu, *Angew. Chem., Int. Ed.*, 2020, **59**, 11800.

 